Synergistic Optimization Enables Large-Area Flexible Organic Solar Cells to Maintain over 98% PCE of the Small-Area Rigid Devices

Guodong Wang, Jianqi Zhang,* Chen Yang, Yuheng Wang, Yi Xing, Muhammad Abdullah Adil, Yang Yang, Lijun Tian, Ming Su, Wuqiang Shang, Kun Lu, Zhigang Shuai, and Zhixiang Wei*

Slot-die coating is generally regarded as the most effective large-scale methodology for the fabrication of organic solar cells (OSCs). However, the corresponding device performance significantly lags behind spin-coated devices. Herein, the active layer morphology, flexible substrate properties, and the processing temperature are optimized synergistically to obtain high power conversion efficiency (PCE) for both the flexible single cells and the modules. As a result, the 1 cm² flexible devices produce an excellent PCE of 12.16% as compared to 12.37% for the spin-coated small-area (0.04 cm²) rigid devices. Likewise, for modules with an area of 25 cm², an extraordinary PCE of 10.09% is observed. Hence, efficiency losses associated with the upscaling are significantly reduced by the synergistic optimization. Moreover, after 1000 bending cycles at a bending radius of 10 mm, the flexible devices still produce over 99% of their initial PCE, whereas after being stored for over 6000 h in a glove box, the PCE reaches 103% of its initial value, indicating excellent device flexibility as well as superior shelf stability. These results, thus, are a promising confirmation the great potential for upscaling of large-area OSCs in the near future.

G. D. Wang, Dr. J. Q. Zhang, C. Yang, Y. H. Wang, Y. Xing, M. A. Adil, Dr. Y. Yang, Prof. K. Lu, Prof. Z. X. Wei
CAS Key Laboratory of Nanosystem and Hierarchical Fabrication
CAS Center for Excellence in Nanoscience
National Center for Nanoscience and Technology
Beijing 100190, P. R. China
E-mail: zhangjq@nanoctr.cn; weizx@nanoctr.cn
G. D. Wang, Prof. Z. G. Shuai
Department of Chemistry
Tsinghua University
Beijing 100084, P. R. China
Y. H. Wang
Frontier Institute of Science and Technology
Xi'an Jiaotong University
Xi'an 710049, P. R. China
Y. Xing
Department of Chemistry
Tianjin University
Tianjin 300072, P. R. China
L. J. Tian, M. Su, W. Q. Shang
Datong Coal Mine Group Co., Ltd
Datong 03 7003, P. R. China

The ORCID identification number(s) for the author(s) of this article can be found under https://doi.org/10.1002/adma.202005153.

In recent years, extensive research attention has been focused on the bulk-heterojunction organic solar cells (OSCs) owing to their admirable attributes such as being lightweight, low-cost, and mechanically flexible, and the ease of large-scale fabrication. Naturally, the power conversion efficiency (PCE) of OSCs has grown rapidly, as the small-area single-junction devices can now produce over 18% PCE.[1–6] However such high PCEs are usually obtained by the spin coating method on rigid substrates (**Figure 1**a) which, due to the associated uneven linear speeds, can be a difficult process to be extended to form large-area devices. Among the different large scale processing methods, the slot-die coating technique (Figure 1a) can be considered as the most effective strategy.[7] Even though the spin coating process is more convenient to operate, excessive waste material and intermittent device processing is always a problem. Conversely, despite its complex processing control, the slot-die coating technique consumes fewer materials and continuous device processing can be realized for flexible substrates.[8] However, a dramatic drop in the PCEs occurs moving from the small-area rigid OSCs to the large-area flexible devices for various complex reasons.[7] First of all, since different coating processes are involved, it is difficult to control the uniformity, thickness, crystallization and morphology of the film for large-area devices as compared to small-area devices. Secondly, the surge in the optical and electrical losses as a consequence of changes in transmittance and conductivity associated with the changing of substrates from rigid to flexible also affects the performance. Finally, the utilization of nonhalogenated solvents in upscale fabrication may also cause efficiency reduction. Therefore, the idea of going from laboratory small-area rigid devices to actual and efficient large-scale application still seems farfetched.

To fulfill the future applications, further studies on the preparation of flexible large-area OSCs are vastly required. In recent years, a lot of work has been done in producing such devices. In 2009, Krebs et al. adopted a roll-to-roll (R2R) process to make flexible OSCs, reaching PCEs of 2.3% and 2.1% for an active area of 4.8 and 120 cm², respectively.[9] In 2017, Bao et al. reported a single strip flexible OSC device via slot-die

Figure 1. a) Sketch of spin coating and slot-die coating. b) The small-area rigid device and large-area flexible device. c) The chemical structures of PTB7-Th, PC$_{71}$BM, and COi8DFIC. d) Optical microscopy and SEM images of the PET/silver-grid substrate. e) Comparison of this work and reported PCEs of flexible devices fabricated by slot-die coating.

technique, reaching up to 5.1% PCE (total device area 10 cm^2) based on PTB7-Th:PPDIE system.[10] The same year, Huang et al. processed series connected OSC modules based on R2R slot-die coating on flexible substrates and achieved PCEs of 5.7% and 4.34% for single cells (2 cm^2) and modules (20 cm^2), respectively.[11] Our group employed a slot-die coating method on poly(ethylene terephthalate)–indium tin oxide (PET–ITO) substrates and fabricated flexible single OSCs as well as modules with two and four serial stripes, producing 5.75%, 5.82%, and 5.18% PCEs, respectively.[12] In early 2019, flexible devices prepared by sequential slot-die coating with efficiencies of 7.11% (1 cm^2) and 6.8% (2 cm^2) were also reported by our group.[13] Likewise, Chen et al. reported flexible devices processed by slot-die printing based on PBDB-T:ITIC, with an efficiency of 9.77% and 8.9% for 1.04 cm^2 single cell and 15 cm^2 module, respectively.[14] However, the width of their single cell was 0.51 cm (less than the common requirement of 1 cm), and as the PCE significantly depends on the width of the single cell, it is difficult to consider these results good or bad as compared to the other systems. The reports of large-area (≥1 cm^2) OSCs with flexible substrates fabricated by slot-die coating technique have been sorted out in Figure 1e, whereas the data list has been provided in the supporting information (Table S1, Supporting

Information). As discussed above, it can be seen that the performance of the devices fabricated on flexible large-area substrates via slot-die coating is significantly lower as compared to the devices fabricated via the spin coating process on small-areas. Thus, the active layer morphology, flexible substrate properties and processing conditions need to be optimized synergistically.

In this work, PTB7-Th:COi8DFIC:PC$_{71}$BM-based ternary system has been employed as not only it is capable of producing high efficiency,[15,16] it is also found to have good solubility in non-halogenated solvents. Although the film-forming kinetics of the slot-die coating is totally different from that of spin coating (Figure 1a), tuning the substrate temperature can enable an optimized molecular arrangement as well as high PCE similar to the spin coating ones. The real images of as-prepared small-area rigid device and large-area flexible OSCs are shown in Figure 1b, whereas the chemical structures of the donor and acceptors are shown in Figure 1c. A non-halogenated solvent, o-xylene has been selected for the fabricating process, while the glass/ITO, PET/ITO, and PET/silver-grid (Figure 1d and Figure S1a, Supporting Information) have been adopted as the transparent electrodes. Likewise, the spin coating and the slot-die (SD) coating methodologies have been employed to coat the active layer on the rigid substrate (inert conditions)

and flexible substrate (in atmosphere), respectively. To reduce the electronic loss, herein, a new type of flexible substrate, PET/silver-grid has been adopted (Figure 1d), replacing the traditional PET/ITO substrate owing to its excellent attributes such as conductivity, light transmission, flexibility, etc.[17–20] The active layer morphology, flexible substrate properties and processing temperature have been optimized synergistically, which enabled large-area flexible OSCs (1 cm^2) to maintain over 98% PCE of the small-area (0.04 cm^2) rigid devices (12.16% vs 12.37%). Furthermore, the flexible OSCs exhibited good flexibility at a bending radius of 10 and 5 mm, as well as superior storage stability after being stored over 6000 h in a glove box. Moreover, 25 cm^2 large-area modules have also been fabricated which obtained an excellent efficiency of over 10%, indicating a great up-scaling probability of this system. To our best knowledge, these are the highest PCEs ever reported for the flexible OSC modules (Figure 1e), while demonstrating minor efficiency losses with the upscaling via slot-die coating methodology.

The absorption spectra of the organic films formed by the spin coating and SD coating methodologies at different temperatures has been shown in **Figure 2**a. The component spectra of PTB7-Th and COi8DFIC at different temperature is shown in Figure S2c (Supporting Information). For the devices fabricated at room temperature, compared with the spin coated films, the SD coated film revealed a big blue shift with the optical absorption edge being reduced from 1050 to 930 nm. Since the optical absorption in the range of 930 to 1050 nm originates from J-type π–π stacking,[21] the molecular packing appears to be quite different between the spin coated and the SD coated films. Interestingly, this J-type π–π stacking got reduced in SD coated films at room temperature. This can be attributed to

the different orientations and different preferred growth direction of COi8DFIC, as its growth might have been kinetically facilitated during the SD-casting process (see the following discussion on morphology). However, from room to elevated temperatures, a big red shift in the optical absorption spectra have been observed. Hence, the films fabricated at 60 and 80 °C are slightly red-shifted as compared to those at 40 °C (absorption edges), whereas the films coated at 100 °C have been blue-shifted as compared to the films formed at 80 °C. In addition, the absorption peak at 850 nm (the primary absorption peak of COi8DFIC film) becomes broader with both blue shift and redshift, going from room temperature to hot casted ones. This indicated that both H- and J-type π–π stackings have formed via tuning the substrate temperature, which is consistent with the reported results.[21] Correspondingly, the EQE curves show a wider spectrum when hot substrates have been employed, especially at 80 °C (shown in Figure 2c), and hence, the J_{sc} of devices coated at 80 °C reaches 26.65 mA cm^{-2}. On the other hand, from 360 to 650 nm, the EQE curve for films coated at 80 °C demonstrate a more convex shape compared with that of the other temperatures, indicating that the photon-to-carrier conversion is dramatically enhanced at this range due to the suppressed crystallization of COi8DFIC (discussed below).

A major difference between the spin coating and the SD coating process is the film formation kinetics. For the spin coating process, the film dries much rapidly and with high shear force as compared to the SD process, where a relatively lower drying rate with weak shear force is observed. Thus, due to the morphology changes during the SD process, a dramatic drop in the PCEs is generally observed. The performances of OSCs based on the rigid and flexible substrate have been listed in
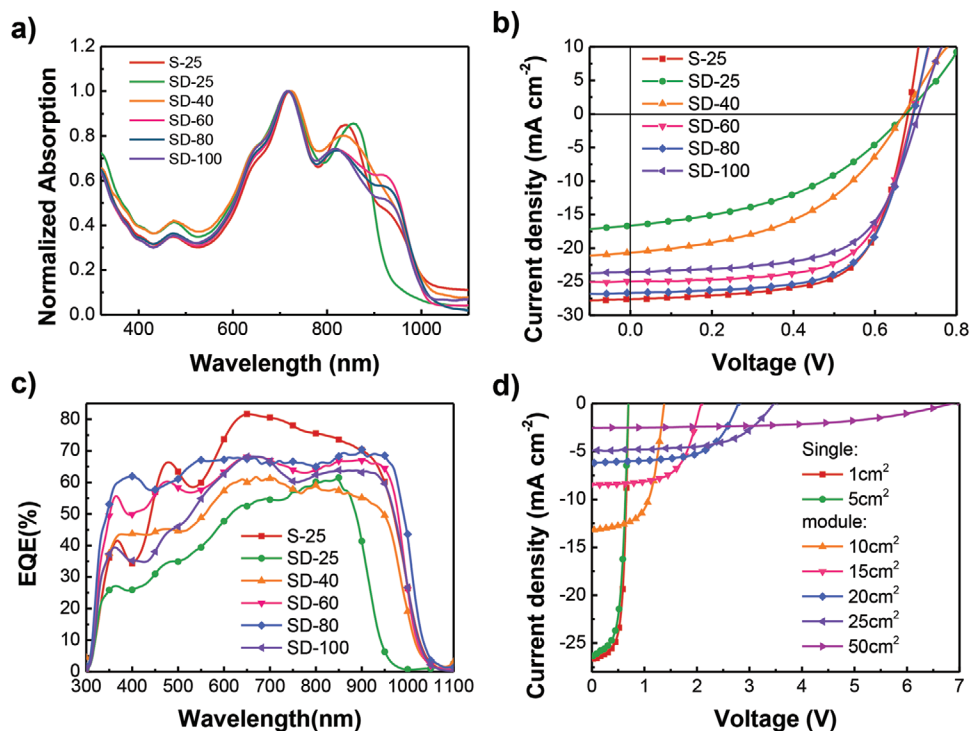
Figure 2. a) Absorption spectra, b) J–V curves of the corresponding devices, c) EQE of PTB7-Th:COi8DFIC:PC$_{71}$BM devices fabricated at different temperatures, and d) vertical phase distribution of PTB7-Th:COi8DFIC:PC$_{71}$BM films coated by slot-die at different temperatures.

**ADVANCED
SCIENCE NEWS**
www.advancedsciencenews.com

**ADVANCED
MATERIALS**
www.advmat.de

Table 1. Performance of devices at different temperatures (area: 1.00 cm^2; inverted devices).

T [°C]	Optimized pump speed/roll speed	V_{oc} [V]	J_{sc} [mA cm^{-2}]	$J_{sc, EQE}$ [mA cm^{-2}]	FF [%]	PCE$_{max}$ [%]	PCE$_{ave}$ [%]
25	1.0	0.675	16.57	16.42	43.12	4.82	4.57 ± 0.24
40	0.75	0.670	20.59	20.12	46.53	6.42	6.26 ± 0.21
60	0.9	0.692	24.99	23.76	65.28	11.29	11.13 ± 0.12
80	0.9	0.694	26.65	25.33	65.75	12.16	12.04 ± 0.13
100	0.7	0.707	23.54	23.46	62.98	10.48	10.27 ± 0.16

Table 1 and Table S2 (Supporting Information). After changing the solvents from CB (literature report) to *o*-xylene, the best performance from small-area rigid devices (0.04 cm^2) came out to be 12.37%, with a V_{oc} of 0.68 V, J_{sc} of 27.61 mA cm^{-2}, and FF of 65.82% (Figure 2b and Table S2, Supporting Information). For PET/ITO substrate, a PCE of 3.05% is attained for a 1 cm^2 device, exhibiting a V_{oc} of 0.678 V, with a significantly lower J_{sc} and FF of 14.54 mA cm^{-2} and 30.96%, respectively, as compared to the small-area devices. Considering the morphology difference and the high crystallinity of the COi8DFIC acceptor, a hot substrate strategy has been applied to optimize the morphology. As a result, at 80 °C, except for the V_{oc} (0.693 V), the J_{sc} and FF both got enhanced to 23.90 mA cm^{-2} and 44.94%, respectively, ultimately producing an increased PCE of 7.44% for the corresponding system. This indicated that the hot substrate strategy has indeed been quite effective in optimizing the morphology and in turn enhancing the device performance (discussed later). However, the current FF still is very low, which might be from the high resistance of the PET/ITO electrodes.

Thus, to improve the conductivity of the flexible substrate, the PET/ITO has been replaced by PET/silver-grid as shown in Figure 1d and Figure S1 (Supporting Information). As a result, the PCE of the PET/silver-grid substrate approached 4.82% at room temperature, showing a 58% enhancement as compared to the PET/ITO substrate as a consequence of enhanced FF (from 30.96% to 43.12%). Thus, to obtain the best performing system, devices with different film thickness at different temperatures have been fabricated by varying the pump speed/roll speed ratios (P/R ratios). The corresponding best performances for the 1 cm^2 flexible devices at 25, 40, 60, 80, and 100 °C have been summarized in Table 1 (Table S3 (Supporting Information) hold the performances of 1 cm^2 flexible devices with different P/R ratios at different temperatures). Interestingly, a significant rise in the PCEs has been observed going from room temperature to 80 °C, after which the PCE starts to reduce slightly till 100 °C. Ultimately, the best PCE of 12.16% with a V_{oc} of 0.69 V, J_{sc} of 26.65 mA cm^{-2}, and a FF of 65.75% has been obtained for devices fabricated at 80 °C for 1 cm^2 devices, which is the highest efficiency recorded for flexible OSCs with an area of 1 cm^2 made by slot-die coating, up to date.

Hence, a remarkable increase in the efficiency has been observed after changing the PET–ITO substrate to PET/silver-grid, which led to an increase in the J_{sc} and FF of the corresponding devices. Although the transmittance of the PET/ITO and PET/silver-grid substrate is almost the same (≥85%), enhanced light harvesting can be achieved in the completed devices based on PET/silver-grid, as confirmed by the EQE results (Figure S2b, Supporting Information). The significant

improvement in the EQE from 300–600 nm range might be from the relatively higher transmittance of PET/silver-grid substrate as shown in Figure S2a (Supporting Information). Therefore, a relatively higher J_{sc} has been observed for the corresponding devices as compared to the PET–ITO substrate. Moreover, the relatively lower resistance of PET/silver-grid substrates (1.5 Ω sq^{-1} vs 30 Ω sq^{-1} for PET/ITO) leads to a significant increase in the FF as well.[22] In summary, the performance of the flexible devices based on PET/silver-grid substrate surpasses that of PET/ITO based substrates, as the former exhibits lower efficiency loss from small-area rigid to large-area flexible devices. Hence, proving that the efficiency losses associated with the upscaling can be significantly reduced by synergistically optimizing the morphology of the active layer and reducing the electrical losses within the flexible substrate.

Similarly, large-area OSC modules have been developed with the PET/silver-grid substrate by carefully designing the slot-die process. The fabricated module product has been shown in Figure 1b, while the coated active layer film has been shown in Figure S1b (Supporting Information), and the schematic diagram of OSC modules has been illustrated in Figure S1c (Supporting Information). Herein six modules with different areas have been fabricated where the single cell has a length of 5 cm and width of 1 cm. Thus, the largest module with 10 sub-cells has an area of 50 cm^2. As shown in **Table 2**, the photovoltaic parameters of all the modules have exhibited excellent performances with PCEs of 11.11% (5 cm^2), 11.01% (10 cm^2), 10.98% (15 cm^2), 10.55% (20 cm^2), 10.09% (25 cm^2), and 9.05% (50 cm^2) respectively, which is indeed an outstanding performance for the large-area flexible OSCs. The J–V curves for the single devices and modules with various areas have been shown in Figure 2d. Since the geometry fill factor of the modules is 77% (the ratio of active area to total area), the corresponding module efficiency were adjusted as 8.48%, 8.45%, 8.12%, 7.76%, and 6.97% for 10, 15, 20, 25, and 50 cm^2 systems, respectively. Based on the current research results, we believe that it is a big step forward in the modularization of flexible organic solar cells, and the industrialization of large-area flexible OSC modules with high-efficiency will be realized in the near future.

To figure out the reasons for this minor yet apparent efficiency loss in the devices, transmission electron microscopy (TEM) and grazing-incidence wide-angle X-ray scattering (GIWAXS) techniques have been employed for analyzing the morphology and crystallinity of the active layers after spin coating and SD coating at different temperatures. For the spin-coated films, the domain size came out to be ≈36 nm as shown in the TEM image (see **Figure 3**a). For the SD coated film at room temperature, domains with a size of ≈49 nm have been

Table 2. Parameters and photovoltaic performance of the modules involved.

Total Area [cm²]	Serial stripes	Single cell area [cm²]	V_{oc} [V]	J_{sc} [mA cm⁻²]	FF [%]	PCE_{max} [%]	PCE_{ave} [%]
1	1	1 × 1	0.694	26.65	65.75	12.16	12.04 ± 0.13
5	1	1 × 5	0.695	26.21	61.01	11.11	11.01 ± 0.08
10	2	1 × 5	1.379	13.21	60.43	11.01	10.71 ± 0.23
15	3	1 × 5	2.085	8.48	62.14	10.98	10.58 ± 0.25
20	4	1 × 5	2.787	6.20	61.09	10.55	10.29 ± 0.18
25	5	1 × 5	3.463	4.93	59.13	10.09	9.81 ± 0.20
50	10	1 × 5	6.852	2.54	51.91	9.05	8.80 ± 0.18

observed as a consequence of the slow drying process. A similar domain size has been observed for the devices at 40 °C. Conversely, as the temperature rises further, a decrease in the domain size and phase separation has been observed, similar to the spin-coated film, which undoubtedly is more reasonable and more conducive to the carrier transportation.

GIWAXS measurements have been further carried out to probe crystallographic changes (Figure 3b shows the 2D GIWAXS patterns for spin coating and SD coating at different temperatures). The corresponding out-of-plane (OOP) and in-plane (IP) cuts have been presented in Figure 3c,d. To index the scattering peaks in the 2D GIWAXS patterns, the single crystal

of COi8DFIC (Figure S3, Supporting Information), obtained by slow diffusion of poor solvent (methanol) in chloroform solution at room temperature,[23] has been analyzed which revealed an interplane spacing for the (010), (100), and (01–1) planes to be 12.88, 10.64, and 9.53 Å, respectively, corresponding to the peaks located at 0.49, 0.594, and 0.64 Å⁻¹, and thus, revealing an interplane spacing of 12.81, 10.57, and 9.81 Å, respectively, as per the GIWAXS data. Hence, the three peaks have been indexed as (010), (100), and (01–1) as shown in Figure 3c. In Figure 3e, different viewing angles of the molecular packing structure have been exhibited to highlight the charge transport channels. It can be seen that the adjacent COi8DFIC
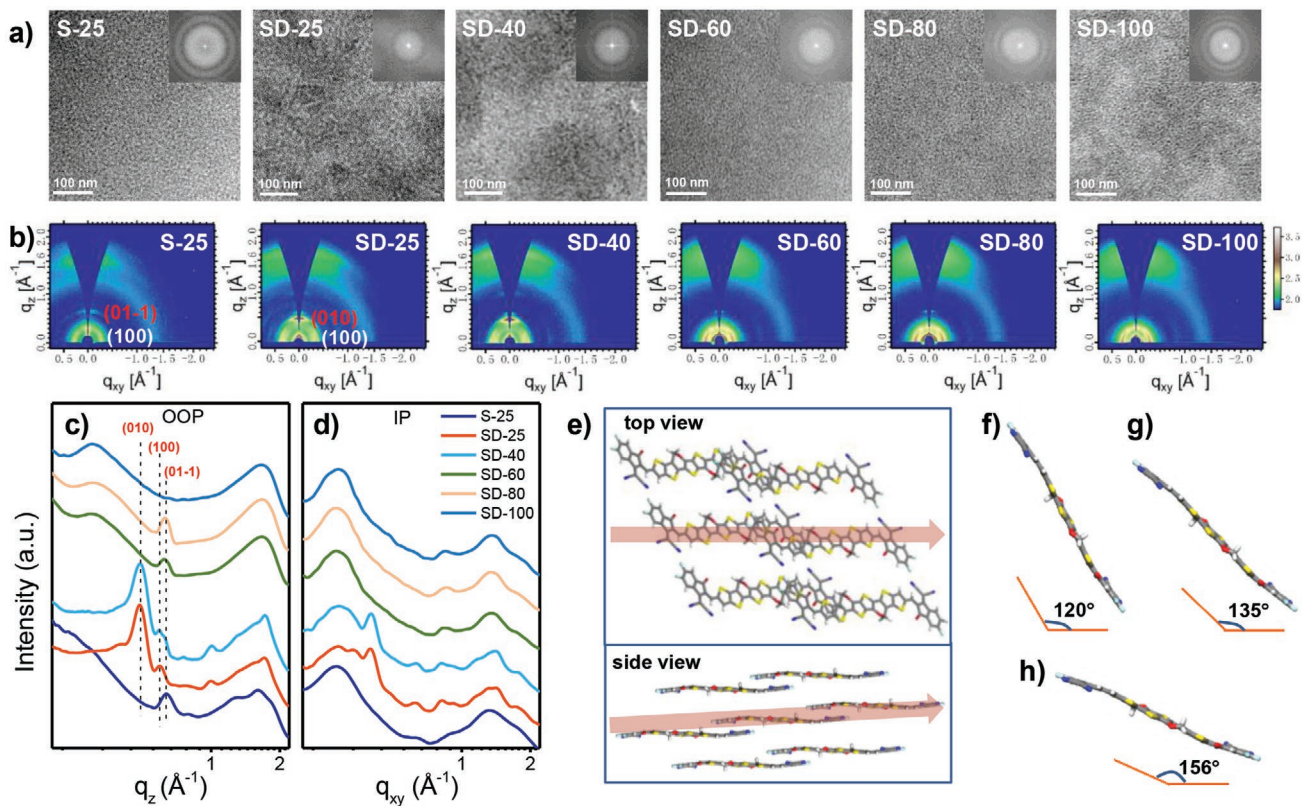
Figure 3. a) TEM images and corresponding FFT patterns (inset images), and b) 2D GIWAXS of PTB7-Th:COi8DFIC:PC₇₁BM films formed by spin coating (S-25) at room temperature and slot-die coating (SD) at different temperatures. c,d) The corresponding out-of-plane (OOP) (c) and in-plane (IP) (d) cuts. e) Molecular packing of COi8DFIC in single crystal, the arrows indicate the best charge transport direction. For the sake of clarity, the alky chains are omitted. f–h) The direction of the molecular backbone with respect to the substrate when (01–1), (010), and (100) planes parallel to the substrate, meanwhile, the angles between the molecular backbone with respect to the substrate are indicated.

**ADVANCED
SCIENCE NEWS**

www.advancedsciencenews.com

**ADVANCED
MATERIALS**

www.advmat.de

molecules are connected parallelly in a head-to-tail way via π–π interaction of the terminal acceptor groups, resulting in a 1D charge transport channel along the backbone packing direction.[24] The arrows indicate the best charge transport direction. Thus, the orientation of the charge transport channel, i.e., the backbone, is critical for getting a high performance. Furthermore, the angles between the charge transport channels with respect to the substrate have been calculated based on the GIWAXS data and single crystal structure (Figure 3f–h). For the spin coated film, the GIWAXS pattern showed weak diffraction arcs from (100) of PTB7-Th and (01–1) of COi8DFIC as indexed in the 2D pattern. Furthermore, a weak and broad (01–1) peak has been observed in the OOP cuts of the spin-coated films. This indicates that the crystallinity of COi8DFIC is relatively low, while the orientation of the molecules is almost perpendicular to the substrate (Figure 3f). This orientation significantly benefits the charge transport, as can be seen from the charge mobility data in Table S4 (Supporting Information). As the coating temperature increases, both the hole mobility and electron mobility increase by an order of magnitude, from 10^{-5} to 10^{-4}, owing to the changes in the crystal orientation. In addition, the devices coated at 80 °C exhibited the most balanced hole and electron mobility, ultimately resulting in the best device performance.

However, a different GIWAXS pattern has been obtained for the SD-coated film at room temperature as the OOP cuts reveal two diffraction peaks at 0.49 and 0.594 Å^{-1} positions, indicating a strong diffraction peak (010), and a weak diffraction peak (100) from COi8DFIC. This means that due to the SD coating influenced slow drying process at room temperature, the COi8DFIC shows high crystallinity and a big crystal size as its growth is kinetically facilitated, which is consistent with the TEM result. Moreover, According to the GIWAXS and the single crystal data, if the (010) and the (100) planes are parallel to the substrate, the charge transport channels would have been tilted by 135° and 156° with respect to the substrate (Figure 3g,h), which is detrimental for the charge transport in the perpendicular direction. This might be the main reason why the SD-coated film at room temperature demonstrates poor performance. Similarly, for the SD-coated films at 40 °C, in addition to (010) and (100) peaks, a weak (01–1) peak has also been observed in the OOP direction, indicating that the three different molecular orientations, as exhibited in Figure 3f–h, are coexisting simultaneously. The molecular re-orientation may result from the temperature-dependent COi8DFIC crystallization, the donor and COi8DFIC interactions, as well as the drying kinetics. With further increasing the temperature to 60 and 80 °C, the 2D GIWAXS patterns not only become similar to the spin-coated ones, but a pronounced (01–1) peak can also be seen in the OOP direction, indicating all the films to have the same orientation (Figure 3f). However, when the processing temperature has been increased to 100 °C, the diffraction peaks of COi8DFIC disappear in 2D GIWAXS patterns, revealing that the crystallization of COi8DFIC is suppressed at higher temperatures during SD coating. Although the GIWAXS data shows that the SD coated COi8DFIC is amorphous in the films at 100 °C, the absorption spectra demonstrate strong H- and J-type π–π stacking that results in broadened absorption range and fine phase separation. This is consistent with the reported binary

system.[21] Hence, the GIWAXS data reveals that the COi8DFIC with optimized orientation is vital for getting high device performance and such optimized orientation can be achieved by tuning the processing temperature during the SD coating, and ultimately, the efficiency losses can be reduced by tuning the morphology.

The flexibility test has been carried out by bending the devices at different radius (R = 10 and 5.0 mm). Generally, if the devices can maintain 90% of the initial efficiency after being bent at a radius of 5 mm for 1000 cycles, the corresponding flexible OSCs are believed to have excellent bending performance.[25–27] The normalized parameters (V_{oc}, J_{sc}, and FF) after every 200 bending cycles, until 1000 cycles have been recorded in Table S3 (Supporting Information). When morphing the flexible OSCs to a cylindrical shape (**Figure 4**a), having a radius of 10 mm, and after 1000 bending cycles, the original (unbent) device performance dropped down from 12.16% to 12.06%, which is 99.20% of its initial value (shown in Figure 4b). Likewise, reducing the radius to 5.0 mm (after 1000 bending cycles) also led to a relatively low PCE loss of 5.87% of its initial value (see Figure S4, Supporting Information). From Figure 4b and Figure S4 (Supporting Information), it can be seen that during the bending process, the V_{oc} and J_{sc} of the flexible devices remain constant and sometimes even increases slightly. However, the small decrease in efficiency can mainly be attributed to the decreased FF during the bending test. Overall, we can draw the conclusion that the mechanical bending performance of our flexible silver-grid OSCs has been outstanding, where even after 1000 bending cycles, the efficiency of the flexible devices remains higher than 94% (R = 5 mm) and over 99% (R = 10 mm) of its initial PCE.

Apart from the excellent bending performance, the storage stability of the flexible PET/silver-grid OSCs has also been remarkable. The flexible devices have been placed inside a nitrogen-filled glove box, while their performance tests have been carried out in air once in a while. To evaluate the device stability, the normalized parameters–time figures are shown in Figure 4c,d, from where it can be seen that during the first 360 h the PCE kept rising till 110% of its initial efficiency. Afterward, the efficiency started to decrease to some extent but remained higher than the initial PCE, and even after 6000 h, the PCE still kept 103% of its initial value. Similarly, spontaneous FF and V_{oc} gains without sacrificing the J_{sc} have been observed, which might have originated from the eliminated energetic disorder and reduced recombination trap.[28] All the stability data mentioned above is based on the flexible silver-grid OSCs having an area of 1 cm^2. For the flexible OSC modules with a larger area, the performance increment has not been so obvious but still has been higher than the original value. Therefore, it can be concluded that if good packaging technology is adopted to isolate water and oxygen, the flexible devices would exhibit good shelf stability for a long time. In light of these extraordinary results; large-area OSC modules with satisfactory high efficiency, outstanding flexibility and remarkable stability, it can be concluded that the fabrication of large-area OSCs will be successfully realized soon.

In summary, we have successfully fabricated large-area flexible OSC devices with low-efficiency losses using the slot-die coating technique, by synergistically optimizing the morphology
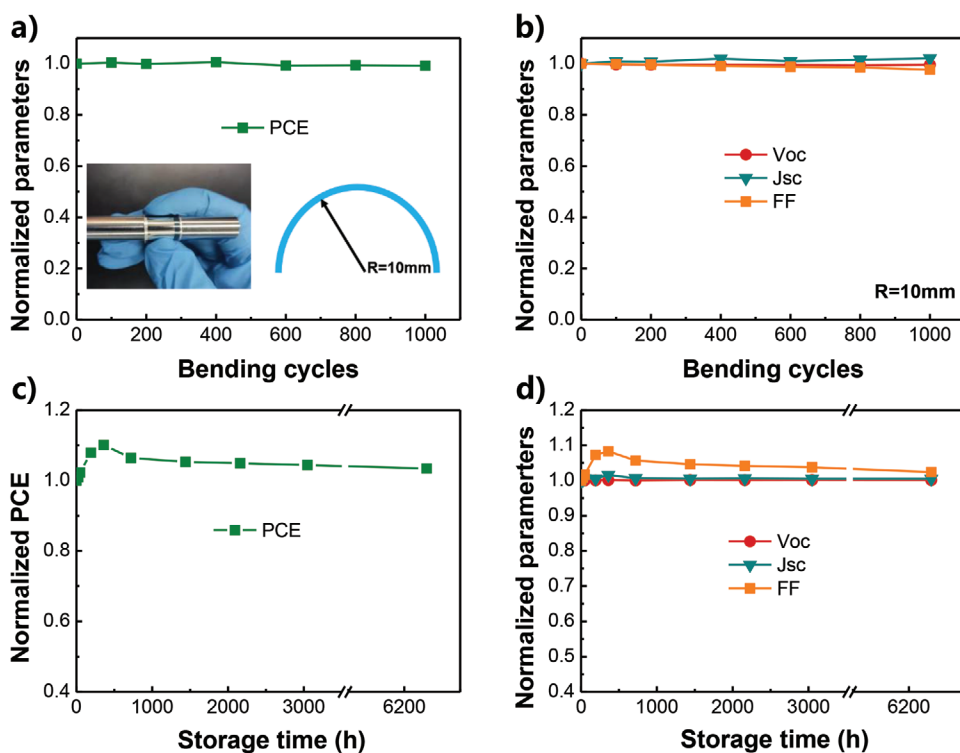
Figure 4. a) Bending stability test. b) Normalized parameters during 1000 bending cycles with a radius of 10 mm. c,d) Storage stability of devices in a nitrogen glove box; the break is due to COVID-19.

of the active layer and reducing the electrical losses within the flexible substrate. By using PET/silver-grid with low resistance and SD casting the active layer at high temperature (80 °C), an extraordinary PCE of 12.16% for single-cell (1 cm^2) has been attained, which is very close to the PCE (12.37%) of the small area (0.04 cm^2) rigid device fabricated by the spin coating process. Similarly, for modules with areas as high as 25 and 50 cm^2, an outstanding PCE of 10.98% and 9.05% has been observed, respectively, that is among the top values for the flexible devices fabricated by slot-die coating methodology. The morphology characterization demonstrates that at elevated temperatures, the crystallization of COi8DFIC molecule gets suppressed, whereas a superior perpendicular molecular orientation and both H- and J-type π–π stacking have been promoted. Furthermore, the hot substrate strategy has been shown as an efficient way to modulate the COi8DFIC-based system. In addition, superior flexibility and storage stability attributes have been observed in the SD coated devices due to the amorphous conformation of the COi8DFIC molecule. Considering such efficient large-area OSC modules, along with their outstanding flexibility and remarkable stability, it can be concluded that the fabrication of large-area OSCs will be successfully realized soon.

Experimental Section

Small-Area Device Fabrication: PTB7-Th was purchased from 1-material Chemscitech Inc. (Canada), while COi8DFIC and PC$_{71}$BM were purchased from Hyper, Inc. (China). All the materials were used as received. For spin coating devices, the glass–ITO substrate (15 Ω sq^{-1}) was purchased from South China Xiang Science & Technology Co., Ltd. The ITO glass

was cleaned by sequential sonication in soap with deionized (DI) water, then in acetone, and finally in isopropyl alcohol for 20 min each. After ultraviolet–ozone (Ultraviolet Ozone Cleaner, Jelight Company, USA) treatment for 5 min, a ZnO electron transport layer was spin-coated at 3000 rpm over the ITO substrate. The concentration of ZnO sol–gel with isopropyl alcohol solvent was set to 15 mg mL^{-1}. The active layer solutions were prepared in *o*-xylene with 1% v/v 1,8-diiodooctane (DIO) as the solvent additive. A polymer concentration of 10 mg mL^{-1} was used to form the blends while maintaining the overall PTB7-Th:COi8DFIC:PCBM ratio at 1:1.05:0.45 w/w. The active layers were spin-coated at 2000 rpm in an N$_2$ glove box at room temperature. At a vacuum level of ≈1.0 × 10^{-6} mbar, a thin layer (5 nm) of MoO$_x$ was deposited as the anode interlayer, whereas 160 nm Ag was deposited as the top electrode. The area of the spin-coated devices was set to 0.04 cm^2.

Large-Area and Module Device Fabrication: Silver-grid patterned on PET substrates (1.5 Ω sq^{-1}, $T \geq 85\%$) was selected as the bottom electrode, upon which the pattern was designed by ourselves and processed by collaborators. A mini-roll coater (FOM Technologies, Denmark) was utilized as the R2R SD coater. The inverted solar cell devices were processed in an ambient atmosphere, using the PET silver-grid/ZnO/active layer/MoO$_x$/Ag structure. PET/silver-grid/ PH1000 hybrid electrodes were fabricated to improve the surface flatness and wettability of the substrates. The highly conductive poly(3,4-ethylenedioxythiophene) polystyrene sulfonate (PEDOT:PSS) (Clevios PH1000, Heraeus, Germany) was diluted with isopropyl alcohol at a ratio of 1:3 v/v and then SD coated on the PET/silver-grid substrates with an injection speed of 10 mL h^{-1} and roller speed of 35 m h^{-1}. The hybrid electrodes were baked at 120 °C for 15 min in ambient air. Then ZnO was coated as the electron transport layer (ETL) by SD coating ZnO sol–gel with isopropyl alcohol solvent (15 mg mL^{-1} concentration), injected at a speed of 4 mL h^{-1} on a roller with a speed of 35 mL h^{-1}. The active layer solutions were prepared in *o*-xylene with polymer concentrations of 10 mg mL^{-1} and 1% v/v 1, 8- diiodooctane (DIO) was added as the additive solvent. The ratio of PTB7-Th:COi8DFIC:PCBM was maintained at 1:1.05:0.45 w/w. After heating the roller to 80 °C, the active layers were

**ADVANCED
SCIENCE NEWS**

www.advancedsciencenews.com

**ADVANCED
MATERIALS**

www.advmat.de

slot-die coated with an injection speed of 5.4 mL h^{-1} and a roller speed of 60 m h^{-1} in ambient conditions. The samples were then transferred into a vacuum evaporation chamber to deposit the top electrode. At a vacuum level of ≈1.0 × 10^{-6} mbar, a thin layer of MoO$_x$ (10 nm) and Ag (160 nm) were thermally evaporated onto the samples with different shaped templates. The active area for single cells was 1 cm^2, 5 cm^2 and for modules were 10, 15, 20, 25, and 50 cm^2.

For flexible devices based on PET–ITO substrates, the PET–ITO substrates were purchased from FOM Technologies, Denmark, having a square resistance of 30 Ω sq^{-1}, while the thickness of ITO is ≈80 nm. Apart from coating PH1000 and annealing for the bottom electrode, the other steps are the same as before.

Performance Measurement of OSCs: The *J–V* characteristics of the devices were assessed under AM 1.5G (100 mW cm^{-1}) with a Newport Thermal Oriel 91159A solar simulator (for single cells) and SAN-EI ELECTRIC XES-1004SE-200S solar simulator (for modules). For both single cells and the modules, the length and width of each sub-cell were determined by using different evaporation masks. Similarly depending upon the flexible substrates as well as the design pattern, the active area of sub-cells was controlled to 10 mm × 10 mm and 10 mm × 50 mm. Interestingly, the performance of the single cells measured with and without a 1 cm^2 mask turned out to be quite similar (Table S5, Supporting Information). Light intensity was calibrated with a Newport Oriel 91150V-KG5 Si-based solar cell and a Newport Oriel PN 91150V Si-based solar cell. *J–V* characteristics were recorded with a Keithley 2400 source meter unit. EQEs were performed in air with an Oriel Newport system (Model 74 125) equipped with a standard Si diode. Monochromatic light was generated from a Newport 300 W lamp source.

Characterization: Film absorption spectra were measured using a UV–visible spectrophotometer (Model UV-3600). Transmission electron microscopy (TEM) images of thin-film morphology were taken using a Tecnai G2 F20 U-TWIN instrument (FEI Co., USA). Grazing-incidence wide-angle X-ray scattering (GIWAXS) analysis was conducted by the XEUSS SAXS/WASX system (Xenocs). The thicknesses of the active layer were measured by using an Alpha-atepD-120 stylus profilometer (Kla-Tencor).

The supplementary crystallographic data for this paper can be obtained free of charge from The Cambridge Crystallographic Data Centre via www.ccdc.cam.ac.uk/data_request/cif.

Conflict of Interest

The authors declare no conflict of interest.

[1] Y. Lin, B. Adilbekova, Y. Firdaus, E. Yengel, H. Faber, M. Sajjad, X. Zheng, E. Yarali, A. Seitkhan, O. M. Bakr, A. El-Labban, U. Schwingenschlogl, V. Tung, I. McCulloch, F. Laquai, T. D. Anthopoulos, *Adv. Mater.* **2019**, *31*, 1902965.

[2] K. Li, Y. S. Wu, Y. M. Li, H. B. Fu, C. L. Zhan, *Sci. China: Chem.* **2020**, *63*, 490.

[3] L. Zhan, S. Li, T.-K. Lau, Y. Cui, X. Lu, M. Shi, C.-Z. Li, H. Li, J. Hou, H. Chen, *Energy Environ. Sci.* **2020**, *13*, 635.

[4] Q. Liu, Y. Jiang, K. Jin, J. Qin, J. Xu, W. Li, J. Xiong, J. Liu, Z. Xiao, K. Sun, S. Yang, X. Zhang, L. Ding, *Sci. Bull.* **2020**, *65*, 272.

[5] Y. Cui, H. Yao, J. Zhang, K. Xian, T. Zhang, L. Hong, Y. Wang, Y. Xu, K. Ma, C. An, C. He, Z. Wei, F. Gao, J. Hou, *Adv. Mater.* **2020**, *32*, 1908205.

[6] Y. Cui, H. Yao, L. Hong, T. Zhang, Y. Tang, B. Lin, K. Xian, B. Gao, C. An, P. Bi, W. Ma, J. Hou, *Natl. Sci. Rev.* **2020**, *7*, 1239.

[7] G. Wang, M. A. Adil, J. Zhang, Z. Wei, *Adv. Mater.* **2019**, *31*, 1805089.

[8] A. S. Gertsen, M. F. Castro, R. R. Søndergaard, J. W. Andreasen, *Flexible Printed Electron.* **2020**, *5*, 014004.

[9] F. C. Krebs, S. A. Gevorgyan, J. Alstrup, *J. Mater. Chem.* **2009**, *19*, 5442.

[10] X. Gu, Y. Zhou, K. Gu, T. Kurosawa, Y. Guo, Y. Li, H. Lin, B. C. Schroeder, H. Yan, F. Molina-Lopez, C. J. Tassone, C. Wang, S. C. B. Mannsfeld, H. Yan, D. Zhao, M. F. Toney, Z. Bao, *Adv. Energy Mater.* **2017**, *7*, 1602742.

[11] Y.-C. Huang, H.-C. Cha, C.-Y. Chen, C.-S. Tsao, *Prog. Photovoltaics* **2017**, *25*, 928.

[12] J. Zhang, Y. Zhao, J. Fang, L. Yuan, B. Xia, G. Wang, Z. Wang, Y. Zhang, W. Ma, W. Yan, W. Su, Z. Wei, *Small* **2017**, *13*, 1700388.

[13] Y. Zhao, G. Wang, Y. Wang, T. Xiao, M. A. Adil, G. Lu, J. Zhang, Z. Wei, *Sol. RRL* **2019**, *3*, 1800333.

[14] X. Meng, L. Zhang, Y. Xie, X. Hu, Z. Xing, Z. Huang, C. Liu, L. Tan, W. Zhou, Y. Sun, W. Ma, Y. Chen, *Adv. Mater.* **2019**, *31*, 1903649.

[15] Z. Xiao, X. Jia, L. Ding, *Sci. Bull.* **2017**, *62*, 1562.

[16] J. Lee, Y.-H. Seo, S.-N. Kwon, D.-H. Kim, S. Jang, H. Jung, Y. Lee, H. Weerasinghe, T. Kim, J. Y. Kim, D. Vak, S.-I. Na, *Adv. Energy Mater.* **2019**, *9*, 1901805.

[17] Y. Li, L. Mao, Y. Gao, P. Zhang, C. Li, C. Ma, Y. Tu, Z. Cui, L. Chen, *Sol. Energy Mater. Sol. Cells* **2013**, *113*, 85.

[18] L. Mao, Q. Chen, Y. Li, Y. Li, J. Cai, W. Su, S. Bai, Y. Jin, C.-Q. Ma, Z. Cui, L. Chen, *Nano Energy* **2014**, *10*, 259.

[19] Y. Li, L. Mao, F. Tang, Q. Chen, Y. Wang, F. Ye, L. Chen, Y. Li, D. Wu, Z. Cui, J. Cai, L. Chen, *Sol. Energy Mater. Sol. Cells* **2015**, *143*, 354.

[20] Y. Han, X. Chen, J. Wei, G. Ji, C. Wang, W. Zhao, J. Lai, W. Zha, Z. Li, L. Yan, H. Gu, Q. Luo, Q. Chen, L. Chen, J. Hou, W. Su, C. Q. Ma, *Adv. Sci.* **2019**, *6*, 1901490.

[21] W. Li, M. Chen, J. Cai, E. L. K. Spooner, H. Zhang, R. S. Gurney, D. Liu, Z. Xiao, D. G. Lidzey, L. Ding, T. Wang, *Joule* **2019**, *3*, 819.

[22] J. D. Servaites, S. Yeganeh, T. J. Marks, M. A. Ratner, *Adv. Funct. Mater.* **2010**, *20*, 97.

[23] R. Zhou, Z. Jiang, C. Yang, J. Yu, J. Feng, M. A. Adil, D. Deng, W. Zou, J. Zhang, K. Lu, W. Ma, F. Gao, Z. Wei, *Nat. Commun.* **2019**, *10*, 5393.

[24] L. Zhu, Z. Tu, Y. Yi, Z. Wei, *J. Phys. Chem. Lett.* **2019**, *10*, 4888.

[25] Y. Li, G. Xu, C. Cui, Y. Li, *Adv. Energy Mater.* **2018**, *8*, 1701791.

[26] W. Song, X. Fan, B. Xu, F. Yan, H. Cui, Q. Wei, R. Peng, L. Hong, J. Huang, Z. Ge, *Adv. Mater.* **2018**, *30*, 1800075.

[27] Y. Sun, M. Chang, L. Meng, X. Wan, H. Gao, Y. Zhang, K. Zhao, Z. Sun, C. Li, S. Liu, *Nat. Electron.* **2019**, *2*, 513.

[28] R. Sun, D. Deng, J. Guo, Q. Wu, J. Guo, M. Shi, K. Shi, T. Wang, L. Xue, Z. Wei, J. Min, *Energy Environ. Sci.* **2019**, *12*, 2518.